LETTER

Intrinsic ferroelectric switching from first principles

Shi Liu[1], Ilya Grinberg[2,3] & Andrew M. Rappe[2]

The existence of domain walls, which separate regions of different polarization, can influence the dielectric[1], piezoelectric[2], pyroelectric[3] and electronic properties[4,5] of ferroelectric materials. In particular, domain-wall motion is crucial for polarization switching, which is characterized by the hysteresis loop that is a signature feature of ferroelectric materials[6]. Experimentally, the observed dynamics of polarization switching and domain-wall motion are usually explained as the behaviour of an elastic interface pinned by a random potential that is generated by defects[7,8], which appear to be strongly sample-dependent and affected by various elastic, microstructural and other extrinsic effects[9–12]. Theoretically, connecting the zero-kelvin, first-principles-based, microscopic quantities of a sample with finite-temperature, macroscopic properties such as the coercive field is critical for material design and device performance; and the lack of such a connection has prevented the use of techniques based on *ab initio* calculations for high-throughput computational materials discovery. Here we use molecular dynamics simulations[13] of 90° domain walls (separating domains with orthogonal polarization directions) in the ferroelectric material $PbTiO_3$ to provide microscopic insights that enable the construction of a simple, universal, nucleation-and-growth-based analytical model that quantifies the dynamics of many types of domain walls in various ferroelectrics. We then predict the temperature and frequency dependence of hysteresis loops and coercive fields at finite temperatures from first principles. We find that, even in the absence of defects, the intrinsic temperature and field dependence of the domain-wall velocity can be described with a nonlinear creep-like region and a depinning-like region. Our model enables quantitative estimation of coercive fields, which agree well with experimental results for ceramics and thin films. This agreement between model and experiment suggests that, despite the complexity of ferroelectric materials, typical ferroelectric switching is largely governed by a simple, universal mechanism of intrinsic domain-wall motion, providing an efficient framework for predicting and optimizing the properties of ferroelectric materials.

In ferroelectric materials, domain walls separate regions with different polarization orientations. In response to an external perturbation that favours one polarization state over another, the domain wall will move to increase the size of the domain favoured by the perturbation, potentially leading to polarization switching of the whole material. The translational motion of the 180° domain wall has been studied experimentally[9,10,12,14] and theoretically[15–18]. The dynamical behaviour of a domain wall is usually understood as an elastic interface moving in a fluctuating pinning potential that is created by defects[7,8]. Under relatively weak electric fields (E), the propagation of domain walls at finite temperature (T) can be described with a creep process[9,10]:

$$v \propto \exp\left[-\frac{U}{k_B T}\left(\frac{E_{C0}}{E}\right)^\mu \right] \qquad (1)$$

where v is the domain-wall velocity, U is a characteristic energy barrier, k_B is Boltzmann's constant, E_{C0} is a critical field at which depinning occurs at 0 K and μ is the dynamical exponent determined by the nature

of the defects. The dynamical exponent $\mu = 1$ is usually ascribed to the random field defects, which break the symmetry of the ferroelectric double-well potential[9,10], whereas $\mu = 0.5$ is an indication of random bond disorder, which locally modifies the symmetric ferroelectric double-well potential depth[11,12]. Another widely used equation that characterizes the switching and domain-wall motion is Merz's law, which takes the form $v = v_0 \exp(-E_a/E)$, where v_0 is the domain-wall velocity under an infinite field and E_a is the temperature-dependent activation field[14,15]. Merz's law can be viewed as a reformulation of equation (1) with $\mu = 1$ and $E_a = UE_{C0}/(k_B T)$. When the electric field becomes larger than the crossing field E_{C0}, the wall experiences a pinning–depinning transition[10], with the velocity becoming temperature-independent and given by:

$$v \propto (E - E_{C0})^\theta \qquad (2)$$

where θ is a velocity exponent that reflects the dimensionality (D) of the wall. A classical theory based on a nucleation-and-growth mechanism was developed by Miller and Weinreich[15] to explain the intrinsic origin of Merz's law and creep behaviour. However, the Miller–Weinreich model assumes the dominant role of depolarization energy during nucleation, which incorrectly leads to an atomically sharp triangular critical nucleus and implausibly high activation fields for nucleation[9,11]. Multiscale simulations for 180° domain walls in defect-free $PbTiO_3$ revealed a square critical nucleus with diffusive and bevelled interfaces that substantially reduces the nucleation barrier and hence leads to much lower activation fields for domain-wall motion, suggesting an intrinsic origin for $\mu = 1$ (ref. 17).

Unlike the motion of 180° domain walls, switching processes in ceramics, thin films and single-crystal ferroelectrics are not well understood. The presence of a variety of extrinsic features, the possible role of ferroelastic effects in non-180° switching and the long (microsecond–millisecond) timescales typically studied for switching make it challenging to relate the observed hysteresis loops to the microscopic properties of ferroelectric materials. Because of the strong clamping effect of the substrate[19,20], the intrinsic dynamics of non-180° domain walls cannot be studied in high-quality ferroelectric thin films; instead, most recent experimental and theoretical studies of non-180° domain walls have focused on static properties[19]. Here, we use a multiscale approach to computationally model the switching process. We first obtain the missing quantitative understanding of the intrinsic dynamics of non-180° domain walls and encapsulate it in a simple and general model for domain-wall speed. The model is then used in coarse-grained simulations on long timescales that enable accurate calculation of ferroelectric-switching hysteresis loops and coercive fields.

We quantitatively estimate the velocity of a 90° domain wall in defect-free $PbTiO_3$ over a wide range of temperatures and electric fields using large-scale molecular dynamics simulations (see Methods). Figure 1 presents the velocity as a function of applied electric field for various temperatures, revealing an intrinsic 'creep–depinning' transition. In the low-field region ($E < 0.5\,\mathrm{MV\,cm^{-1}}$), the velocity strongly depends on temperature and has a strong nonlinear dependence on the electric field. In the high-field region ($E > 0.5\,\mathrm{MV\,cm^{-1}}$), the temperature

[1]Geophysical Laboratory, Carnegie Institution for Science, Washington DC 20015, USA. [2]The Makineni Theoretical Laboratories, Department of Chemistry, University of Pennsylvania, Philadelphia, Pennsylvania 19104, USA. [3]Department of Chemistry, Bar-Ilan University, Ramat Gan 5290002 Israel.
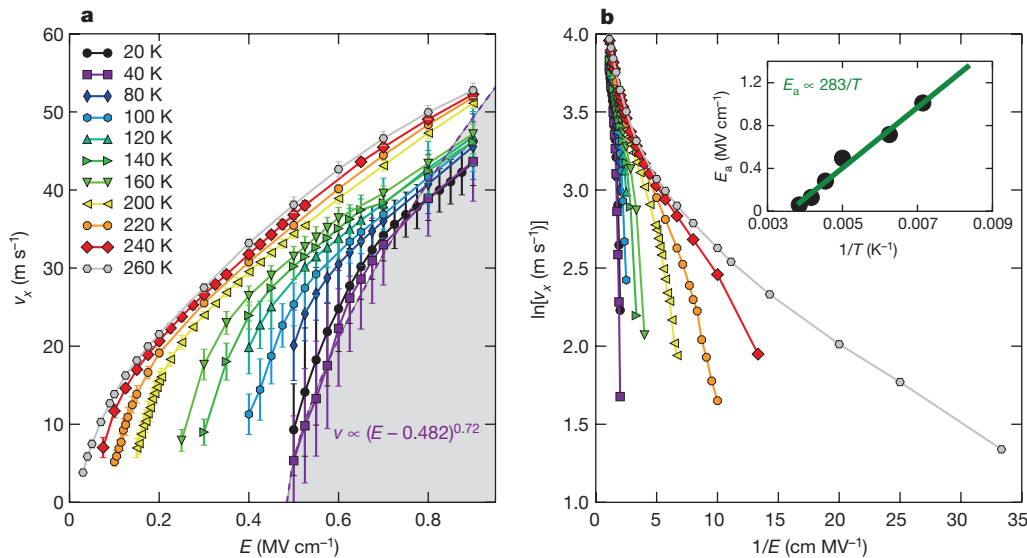
Figure 1 | Domain-wall velocity from molecular dynamics simulations. a, Temperature (T)- and field (E)-dependent domain-wall velocity (v_x) data reveal an intrinsic creep–depinning transition. The domain-wall velocity data at 40 K are in the flow region (shaded area) and are fitted to equation (2). We find $\theta = 0.72$, $E_{C0} = 0.482$ MV cm^{-1} (dashed purple line, boundary of the shaded area). The solid lines are guides for the eye. The error bars are standard deviations of v_x. **b**, Plot of $\ln(v_x)$ versus $1/E$ curves for different temperatures (see legend in **a**). The inset shows the temperature dependence of the activation field $E_a = UE_{C0}/(k_B T)$ in the creep-like region at low fields.

dependence of the domain-wall velocity becomes weaker, as seen by the overlap of the velocity data obtained at different temperatures. Plotting $\ln(v)$ versus $1/E$ (Fig. 1b), we find that $\ln(v)$ has a linear relationship with $1/E$ in the low-field region. This confirms that for relatively low electric fields and high temperatures the velocity of the 90° domain wall follows Merz's law ($\mu = 1.0$), showing a creep-like response even in the absence of defects. The inset in Fig. 1b shows the temperature dependence of the activation field $E_a = UE_{C0}/(k_B T)$ above 140 K. The nearly linear relationship between E_a and $1/T$ shows that UE_{C0}/k_B is temperature-independent in the creep-like region with a value of 283 K MV cm^{-1}. By fitting the velocity data at 40 K with equation (2), we find that $\theta = 0.72$ and $E_{C0} = 0.48$ MV cm^{-1}. The crossing field for the 90° domain wall is lower than that for the 180° domain wall (1 MV cm^{-1}) in Pb(Zr, Ti)O$_3$ (PZT) thin films[10]; this is expected, because *ab initio* calculations have shown that the 90° domain wall in PbTiO$_3$ is lower in energy than the 180° domain wall in PZT[16]. The values of the dynamical exponent are the same ($\mu = 1$) for 90° and 180° domain walls[17]. This indicates a universal intrinsic response for ferroelectric domain walls under low driving force. The observed intrinsic creep–depinning transition can be explained with a nucleation-and-growth mechanism. At low fields, the large size of the critical nucleus and the high nucleation barrier relative to thermal fluctuations make nucleation the rate-limiting step and lead to an Arrhenius dependence of the velocity in the creep region. At high fields, the nucleus size and nucleation barrier approach zero and the domain-wall velocity is growth dominated, resulting in near-linear dependence on electric fields and a weak temperature dependence.

We now develop an analytical model for nucleation at a non-180° domain wall based on our molecular dynamics simulations for 90° domain walls. As shown in Fig. 2a, a 90° domain wall in x–y coordinates can be viewed as a special 180° domain wall in X–Y coordinates: the polarization component parallel to the domain wall (P_Y) is reversed by 180° across the boundary, while the polarization component perpendicular to the domain wall (P_X) remains almost unchanged (bottom of Fig. 2a). This transformation allows us to treat all types of non-180° domain walls as a 180° domain wall and allows a convenient estimate of the relative energies of different types of domain walls based on the Landau–Ginzburg–Devonshire (LGD) expression for the energy per unit area (σ) of the 180° domain wall (σ_{180DW}). Detailed examinations of nucleation events at the domain wall ($X = 0$) at low temperature ($T = 20$ K) reveal a diamond-like nucleus in the Y–Z plane (Fig. 2b), with substantial diffuseness at the boundary characterized by a gradual polarization change. With this microscopic picture of nucleation, we use LGD theory to relate the nucleation energy to the fundamental characteristics of the material (see Methods). The nucleation energy

U_{nuc} includes two important energy terms: polarization–electric-field coupling (PE) and interfacial energy. Contrary to the assumption of the classical Miller–Weinreich model, the depolarization energy is quite small and does not make a substantial contribution to the nucleation energy (see Methods for a detailed analysis of elastic and depolarization energy).

At the lowest approximation, P_X and P_Z remain unchanged across the domain wall and, therefore, the nucleation energy depends only on P_Y. The profile of P_Y for a domain wall containing a nucleus of size $l_1 \times l_2 \times l_3$ can be described as:

$$P_Y = \frac{2P_s}{\sqrt{2}} f(X, l_1, \delta_1) f(Y+Z, \sqrt{2}l_2, \delta_2) f(Y-Z, \sqrt{2}l_3, \delta_3) + \frac{P_s}{\sqrt{2}} g(X, l_1, \delta_1) \quad (3)$$

where $f(x, l, \delta) = \frac{1}{2}\left[\tanh\left(\frac{x+l/2}{\delta/2}\right) - \tanh\left(\frac{x-l/2}{\delta/2}\right)\right]$, $g(x, l, \delta) = \tanh\left(\frac{x-l/2}{\delta/2}\right)$,

P_s is the bulk polarization and δ_i characterizes the diffuseness of the nucleus along direction i. Figure 2c shows the polarization profile in the Y–Z and X–Y planes generated by equation (3). Evaluating this P_Y profile in the LGD energy expression for different parameter values (l_1 and l_2) allow us to identify the critical nucleus size and to estimate the nucleation activation energy (ΔU_{nuc}). According to Avrami theory of transformation kinetics, ΔU_{nuc} can be related to the activation field in Merz's law as $E_a \approx \frac{1}{D+1} \frac{\Delta U_{nuc}}{k_B T} E$, where D is the dimensionality[17]. By applying this relation with $D = 2$ and using parameters (see Methods) obtained from our classical bond-valence potential, we obtain E_a values for a range of temperatures. As shown in Fig. 2d, the activation fields predicted from the analytical model agree well with molecular dynamics results. To apply the model to other types of non-180° domain walls, only a simple modification of the input parameters is required, with the necessary values obtained from first-principles density functional theory (DFT) calculations of the particular domain wall (see Methods).

The availability of an analytical model that uses DFT inputs enables rapid estimation of hysteresis loops and coercive fields (E_c; see Methods). Because the structure and polarization of Ti-rich PZT are similar to those of PbTiO$_3$, we compare the simulated values of the PbTiO$_3$ E_c to various experimental values for PZT materials. We find that our theoretical coercive fields (Fig. 3a) using parameters of 90°-domain-wall motion agree well over a large frequency range with the experimental E_c values (5–20 kV cm^{-1})[21–24]. The E_c values based on 180°-domain-wall motion are quite large and exhibit the correct frequency dependence (Fig. 3c), in agreement with experimental results obtained in thin films (with thickness larger than the critical size of the nucleus)[25]. This suggests that the 180° switching in ceramics proceeds via sequential 90°-domain-wall motion[23], owing to the much smaller
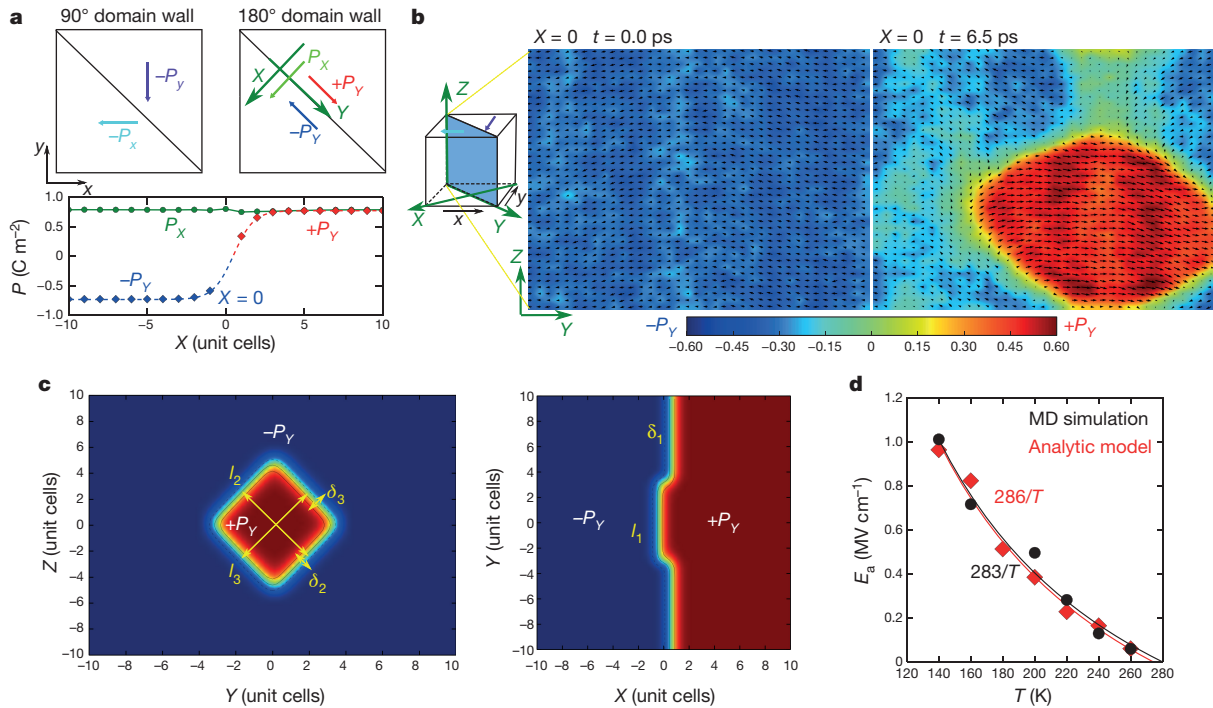
Figure 2 | LGD model of nucleation at domain walls. a, Schematic of mapping a 90° domain wall in x–y coordinates to a 180° domain wall in X–Y coordinates. The bottom panel shows the polarization P profile of a 90° domain wall in X–Y coordinates. The change in P_X across the domain wall ($X = 0$) is small. **b**, Simulated nucleation process at the domain wall in the Y–Z plane (blue-shaded plane in the schematic). The black arrows scale with the local dipole magnitudes of each unit cell in the Y–Z plane. The background of each arrow is coloured on the basis of the magnitude of the Y component of the local dipole. At $t = 0$ ps, the Y–Z interface at

$X = 0$ has dipoles aligned along $-Y$. In the presence of electric field, a diamond-like nucleus forms at $t = 6.5$ ps. **c**, Polarization profile of a nucleus generated by equation (3). The size of the nucleus is defined as $l_1 \times l_2 \times l_3$; $\delta_{1,2,3}$ characterize the diffusiveness of the polarization. **d**, Comparison of the activation fields E_a obtained from molecular dynamics (MD) simulations with the results of the LGD model. The analytical model reproduces molecular dynamics activation fields using bond-valence-potential-based parameters together with the molecular dynamics temperature dependence of local polarization.
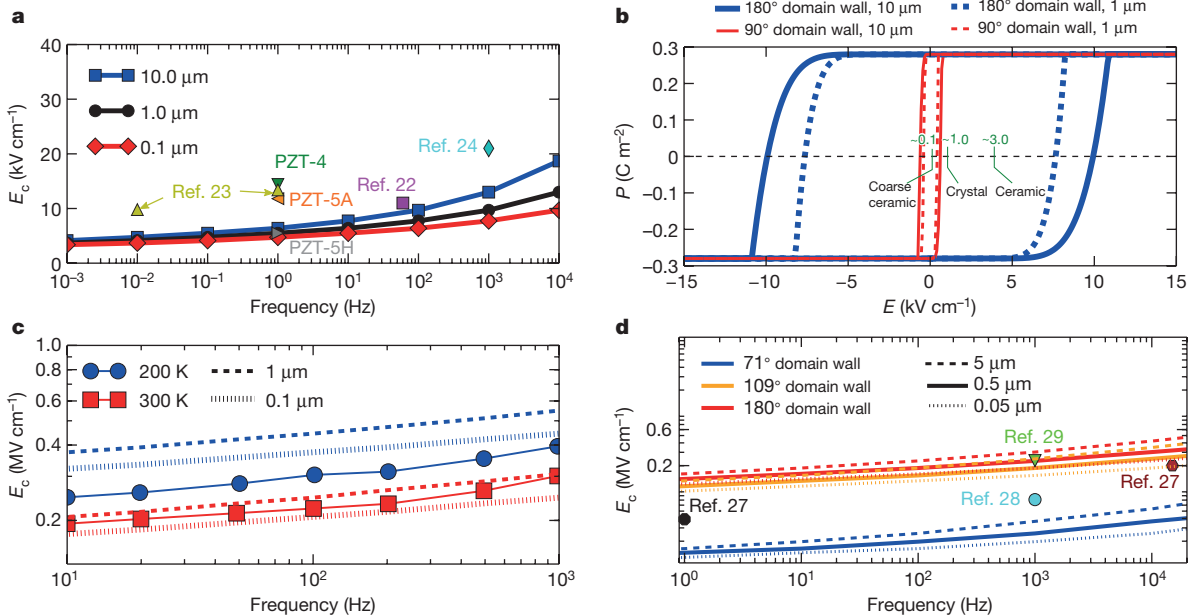

Figure 3 | Hysteresis loops and coercive fields for several materials simulated using first-principles data. a, Simulated frequency dependence of coercive fields E_c for PZT ceramics for various domain sizes (see legend) at 300 K. Theoretical values are comparable to various experimental values[22–24] in ceramics. PZT-4, -5A and -5H refer to different PZT ceramics in ref. 21. **b**, Hysteresis loops of BaTiO$_3$ with a domain size of 1 μm (dashed lines) and 10 μm (coarse grain). The green labels refer to experimental values of coercive fields. **c**, Frequency- and

temperature-dependent coercive fields for PZT thin films. Experimental data (solid lines with filled circles and squares) are taken from ref. 25. A domain size of 0.1 μm (vertically dashed lines) and 1 μm (dashed lines) is used to obtain the theoretical values. **d**, Theoretical coercive fields for different domain walls in BiFeO$_3$ with a domain size of 0.5 μm (solid lines), 0.05 μm (vertically dashed lines) and 5 μm (dashed lines), compared to experimental values[27–29].

intrinsic nucleation barrier at the 90° domain wall. Thus, the switching and coercive fields in PZT are largely determined by the intrinsic properties of the appropriate domain-wall-motion mechanism. Similarly to the PZT results, we find that switching in BaTiO$_3$ ceramics is governed by the motion of 90° domain walls (Fig. 3b), with the predicted coercive field of around $0.1\,kV\,cm^{-1}$ at 300 K close to the experimental value for coarse-grain BaTiO$_3$ ceramics[26].

Polarization reversal in BiFeO$_3$ is another test of our model, owing to the importance of octahedral rotations and the presence of three types of domain walls in rhombohedrally polarized BiFeO$_3$. DFT calculations revealed that the 71° domain wall has the highest energy, followed by the 180° domain wall, with the lowest energy for the 109° domain wall. The higher energy of the 71° domain wall is attributed to the mismatch of oxygen octahedral rotations across the domain boundary. We introduce a second order parameter (oxygen octahedral rotation, Θ) into our LGD-based nucleation-and-growth model (see Methods). Using DFT domain-wall energies, our analytical model predicts that E_c is lowest for the 71° domain wall, followed by the 109° and 180° domain walls. The predicted coercive fields for 180° domain walls are comparable with experimental values in thin films[27–29]. The ability of our simple analytical model to estimate E_c accurately indicates that the value of the coercive field is largely determined by the intrinsic properties of the material, with the nucleation barrier on the domain wall controlling the dynamics of polarization reversal.

The dominant role of intrinsic domain-wall motion explains the consistent differences in E_c of the tetragonal and rhombohedral ferroelectrics. For example, an increase in E_c of approximately 80% is observed across the rhombohedral−tetragonal compositional phase transition at the morphotropic phase boundaries in lead-free (Ba, Ca) TiO$_3$-Ba(Zr, Ti)O$_3$ and Bi-rich BiScO$_3$-Bi(Zr, Ti)O$_3$-PbTiO$_3$ ceramic systems[30]. Analysis of our LGD nucleation model incorporating the changes in octahedral rotations across the 71° domain wall shows that the ratio of the coercive fields for 90° and 71° domain walls is approximately two (see Methods). This suggests that the switching in rhombohedral and tetragonal ferroelectrics proceeds via a multistep switching mechanism that involves a series of 71° and 90° steps, respectively, and that the higher E_c of the tetragonal ferroelectrics is a direct consequence of the larger nucleation energy for 90°-domain-wall motion. The unified framework presented here relates microscopic zero-kelvin quantities to macroscopic material parameters at finite temperature and thus suggests an avenue for rational material design.

1. Xu, R., Karthik, J., Damodaran, A. R. & Martin, L. W. Stationary domain wall contribution to enhanced ferroelectric susceptibility. *Nat. Commun.* **5**, 3120 (2014).
2. Chaplya, P. M. & Carman, G. P. Dielectric and piezoelectric response of lead zirconate–lead titanate at high electric and mechanical loads in terms of non-180° domain wall motion. *J. Appl. Phys.* **90**, 5278–5286 (2001).
3. Karthik, J. & Martin, L. Pyroelectric properties of polydomain epitaxial Pb(Zr$_{1−x}$Ti$_x$)O$_3$ thin films. *Phys. Rev. B* **84**, 024102 (2011).
4. Seidel, J. *et al.* Conduction at domain walls in oxide multiferroics. *Nat. Mater.* **8**, 229–234 (2009).
5. Liu, S. *et al.* Ferroelectric domain wall induced band gap reduction and charge separation in organometal halide perovskites. *J. Phys. Chem. Lett.* **6**, 693–699 (2015).
6. Jin, L., Li, F. & Zhang, S. Decoding the fingerprint of ferroelectric loops: comprehension of the material properties and structures. *J. Am. Ceram. Soc.* **97**, 1–27 (2014).
7. Ioffe, L. B. & Vinokur, V. M. Dynamics of interfaces and dislocations in disordered media. *J. Phys. C* **20**, 6149–6158 (1987).
8. Chauve, P., Giamarchi, T. & Le Doussal, P. Creep and depinning in disordered media. *Phys. Rev. B* **62**, 6241–6267 (2000).
9. Tybell, T., Paruch, P., Giamarchi, T. & Triscone, J.-M. Domain wall creep in epitaxial ferroelectric Pb(Zr$_{0.2}$Ti$_{0.8}$)O$_3$ thin films. *Phys. Rev. Lett.* **89**, 097601 (2002).
10. Jo, J. *et al.* Nonlinear dynamics of domain-wall propagation in epitaxial ferroelectric thin film. *Phys. Rev. Lett.* **102**, 045701 (2009).
11. Paruch, P., Giamarchi, T., Tybell, T. & Triscone, J.-M. Nanoscale studies of domain wall motion in epitaxial ferroelectric thin films. *J. Appl. Phys.* **100**, 051608 (2006).
12. Pertsev, N. A. *et al.* Dynamics of ferroelectric nanodomains in BaTiO$_3$ epitaxial thin films via piezoresponse force microscopy. *Nanotechnology* **19**, 375703 (2008).
13. Liu, S., Grinberg, I., Takenaka, H. & Rappe, A. M. Reinterpretation of the bond-valence model with bond-order formalism: an improved bond-valence-based interatomic potential for PbTiO$_3$. *Phys. Rev. B* **88**, 104102 (2013).
14. Merz, W. J. Domain formation and domain wall motions in ferroelectric BaTiO$_3$ single crystals. *Phys. Rev.* **95**, 690–698 (1954).
15. Miller, R. C. & Weinreich, G. Mechanism for the sidewise motion of 180° domain walls in barium titanate. *Phys. Rev.* **117**, 1460–1466 (1960).
16. Meyer, B. & Vanderbilt, D. Ab initio study of ferroelectric domain walls in PbTiO$_3$. *Phys. Rev. B* **65**, 104111 (2002).
17. Shin, Y.-H., Grinberg, I., Chen, I.-W. & Rappe, A. M. Nucleation and growth mechanism of ferroelectric domain-wall motion. *Nature* **449**, 881–884 (2007).
18. Liu, S., Grinberg, I. & Rappe, A. M. Exploration of the intrinsic inertial response of ferroelectric domain walls via molecular dynamics simulations. *Appl. Phys. Lett.* **103**, 232907 (2013).
19. Pramanick, A., Prewitt, A. D., Forrester, J. S. & Jones, J. L. Domains, domain walls and defects in perovskite ferroelectric oxides: a review of present understanding and recent contributions. *Crit. Rev. Solid State Mater. Sci.* **37**, 243–275 (2012).
20. Gao, P. *et al.* Atomic-scale mechanisms of ferroelastic domain-wall-mediated ferroelectric switching. *Nat. Commun.* **4**, 2791 (2013).
21. Hooker, M. W. *Properties of PZT-based Piezoelectric Ceramics Between −150 and 250 °C*. Report No. NASA/CR-1998-208708, http://ntrs.nasa.gov/search.jsp?R=19980236888 (NASA, 1998).
22. Lente, M. & Eiras, J. 90° domain reorientation and domain wall rearrangement in lead zirconate titanate ceramics characterized by transient current and hysteresis loop measurements. *J. Appl. Phys.* **89**, 5093–5099 (2001).
23. Lente, M., Picinin, A., Rino, J. & Eiras, J. 90° domain wall relaxation and frequency dependence of the coercive field in the ferroelectric switching process. *J. Appl. Phys.* **95**, 2646–2653 (2004).
24. Kong, L. & Ma, J. PZT ceramics formed directly from oxides via reactive sintering. *Mater. Lett.* **51**, 95–100 (2001).
25. Yang, S. M. *et al.* ac dynamics of ferroelectric domains from an investigation of the frequency dependence of hysteresis loops. *Phys. Rev. B* **82**, 174125 (2010).
26. Wu, K. & Schulze, W. A. Effect of the ac field level on the aging of the dielectric response in polycrystalline BaTiO$_3$. *J. Am. Ceram. Soc.* **75**, 3385–3389 (1992).
27. Wang, J. *et al.* Epitaxial BiFeO$_3$ multiferroic thin film heterostructures. *Science* **299**, 1719–1722 (2003).
28. Shelke, V. *et al.* Reduced coercive field in BiFeO$_3$ thin films through domain engineering. *Adv. Mater.* **23**, 669–672 (2011).
29. Guo, E.-J., Dörr, K. & Herklotz, A. Strain controlled ferroelectric switching time of BiFeO$_3$ capacitors. *Appl. Phys. Lett.* **101**, 242908 (2012).
30. Suchomel, M. R. *Greater Functionality of Bismuth and Lead Based Perovskites*. PhD thesis, Univ. Pennsylvania, http://repository.upenn.edu/dissertations/AAI3179819 (2005).

Author Contributions S.L., I.G. and A.M.R. designed and analysed the simulation approaches. S.L. performed the molecular dynamics simulations. All authors discussed the results and implications of the work and commented on the manuscript at all stages.

METHODS

Molecular dynamics simulations of 90° domain walls. To understand the intrinsic dynamics of non-180° domain walls, we study the motion of the 90° domain wall in defect-free PbTiO$_3$ as an example and then generalize the obtained results to other types of non-180° domain walls. We perform constant-temperature constant-pressure (NPT; N is the (constant) number of particles) molecular dynamics simulations over a wide range of temperatures and electric fields using a bond-valence-based classical potential and extract velocity data for the 90° domain wall[13,18,31,32]. We use a $40 \times 40 \times 40$ supercell with the polarization direction changing from $[0\bar{1}0]$ to $[\bar{1}00]$ across the boundary (Extended Data Fig. 1a). Owing to the use of an orthorhombic supercell, the domains are homogeneously strained, making the relative angle between the orientations of the polarization axes of neighbouring domains exactly 90°, rather than $2\arctan(a/c)$ as is geometrically required for a tetragonal ferroelectric with short-axis lattice constant a and long-axis lattice constant c. The electric field is applied along the [100] direction; this will cause the domain wall to move along the [110] direction (with velocity v_{DW}) as a result of the 90° switching of $[\bar{1}00]$ dipoles to $[0\bar{1}0]$ dipoles at the domain boundary (Extended Data Fig. 1b). When dipoles in one layer of unit cells are switched by 90°, the wall moves by $\sqrt{a^2 + c^2}/2$, and the cells initially with their long axis (c) along [100] will now have their short axis (a) along [100], causing $L_{[100]}$ (the cell dimension along [100]) to be reduced by $(c - a)$ (Extended Data Fig. 2a). Therefore, the domain-wall velocity v_{DW} can be estimated from the change in the cell dimension d$L_{[100]}$ using:

$$v_{DW} = \frac{dL_{[100]}}{2dt} \frac{\sqrt{a^2 + c^2}}{2(c - a)} = v_x \frac{\sqrt{a^2 + c^2}}{2(c - a)}$$

with $v_x = dL_{[100]}/2dt$ (the factor of 1/2 is due to the presence of two walls in the simulated supercell). Owing to the stochastic behaviour of nucleation, 20 simulations with slightly different initial structures are carried out for a given temperature and electric field to obtain the velocity average and standard deviation.

It is known that for PbTiO$_3$ the values of the lattice constants depend on temperature. The lattice constants of PbTiO$_3$ are calculated under different temperatures with molecular dynamics simulations; we find that $\sqrt{a^2 + c^2}/[2(c - a)]$ depends on the temperature weakly and is in the 5–6 range (Extended Data Fig. 2b). This temperature dependence has a different origin from the temperature dependence of the domain-wall velocity. For the polarization switching process, the relevant kinetic quantity is v_{DW}/a, which is the effective (switching-related) domain-wall velocity (v_{eff}) in terms of the unit-cell lattice constant a. Therefore, to connect the domain-wall velocity at a given temperature with the experimentally observed switching rate estimated from the switching current, the obtained velocity v_{DW} must be divided by the lattice constant at that particular temperature. We find that v_{eff} exhibits the temperature dependence predicted by equation (1). Owing to the temperature dependence of the lattice constants, the domain-wall velocity measured by v_{DW} deviates somewhat from equation (1). We consider v_{eff} as the intrinsic velocity of the domain wall. Nevertheless, when studying the effect of the electric field on switching at a given temperature, v_x can also be used because it differs from the intrinsic, switching-related domain-wall velocity v_{eff} by a constant multiplicative factor for each temperature. The temperature and field dependence of v_x are presented in Fig. 1 because v_x is the quantity that is most easily and directly obtained from our molecular dynamics simulations. A v_x of 10–50 m s^{-1} corresponds to a domain-wall velocity of 50–250 m s^{-1} or a change in supercell dimension of 1–5 Å per 10 ps—about 4–20 unit cells per 10 ps. All simulations are carried out for 10–50 ps and therefore allow domain-wall movement that can be detected by examination of the changes in the supercell dimensions and total polarization. Our approach for extracting the domain-wall velocity from the change in supercell dimension resembles the experimental switching-current measurement. Experimentally, the domain-wall velocity is extracted by measuring the switching current, which is equivalent to dP/dt. We find from molecular dynamics simulations that v_x scales linearly with dP_x/dt for various temperatures (Extended Data Fig. 2c), showing that v_x is a good indicator of domain-wall velocity for theory–experiment comparison.

The thermal broadening of domain walls is taken into account in finite-temperature molecular dynamics simulations. Increased thermal broadening of the wall diminishes the polarization at the interface of the two domains, leading to a lower nucleation energy, faster domain-wall motion and a lower coercive field. As the temperature approaches the critical temperature, the coercive field is expected to become low, and the domain-wall motion will take place in the flow regime even at low fields. Additionally, the smearing out of the domain wall may lead to a transition from layer-by-layer switching to multilayer switching whereby several unit cells in adjacent layers switch simultaneously.

LGD nucleation model. The nucleation energy U_{nuc} that captures the most important energy terms can be expressed as $U_{nuc} = \Delta U_E + \Delta U_i$ where the polarization-field coupling term ΔU_E is:

$$\Delta U_E = -E \int_{-\infty}^{\infty} dX \int_{-\infty}^{\infty} dY \int_{-\infty}^{\infty} dZ[P_{nuc}(X, Y, Z) - P_{DW}(X, Y, Z)] \quad (4)$$

and the interfacial energy ΔU_i is:

$$\Delta U_i = \int_{-\infty}^{\infty} dX \int_{-\infty}^{\infty} dY \int_{-\infty}^{\infty} dZ \{ [U_g(P_{nuc}) + U_{loc}(P_{nuc})] - [U_g(P_{DW}) + U_{loc}(P_{DW})] \}$$

Here $P_{nuc}(X, Y, Z)$ and $P_{DW}(X, Y, Z)$ are the polarization profiles of a domain wall with and without the nucleus, respectively. U_{loc} is the local energy penalty due to the deviation of the local polarization from the ground-state bulk value (P_s): $U_{loc}(P) = A_{loc}[1 - (P/P_s)^2]^2$, where A_{loc} is the energy difference between the ferroelectric phase and the paraelectric phase. U_g is the gradient energy due to the polarization changes ($\partial_j P_i$) at the domain wall: $U_g(P_i) = \sum_{ij} g_{ij}(\partial_j P_i)^2$, where g_{ij} is the coefficient for the gradient of the ith component of P along direction j. The value of g_{ij} can be derived from the energy and diffusiveness of the domain wall. The contributions from elastic strain energy (ε^2) and strain–polarization coupling (εP^2) terms could be implemented into equation (3). However, we find that the elastic energy change is not significant (see below) and is therefore omitted in the following analysis.

Elastic energy contribution to nucleation energy. We calculate the effective lattice constants (defined in Extended Data Fig. 1a) in X–Y coordinates and find that they remain almost unchanged across the domain wall (Extended Data Fig. 3a). This finding suggests that the elastic energy cost at domain boundaries is not significant in an ideal crystal. Extended Data Fig. 3b, c shows the distributions of strain gradient in the presence of a diamond-like nucleus (illustrated in Fig. 2b). It can be seen that the unit cells of the nucleus have essentially the same lattice constants as the rest of the PbTiO$_3$ unit cells at the domain wall. Therefore, the elastic energy contribution to the nucleation energy (change in elastic energy during nucleation) is negligible and does not have to be treated explicitly. We have therefore omitted explicit strain and strain–polarization coupling terms from our LGD nucleation model at the lowest approximation. Additionally, although the LGD theory presented in the main text does not explicitly refer to elastic interactions, these are included implicitly. It can be shown that inclusion of strain and strain–polarization coupling terms merely renormalizes the fourth-order LGD parameter. Because the parameters for the LGD model are obtained from DFT calculations in which strain polarization coupling is included, these elastic energetics are included in the A_{loc} parameter that specifies the dependence of local energy on local polarization. (Similarly, because the supercell size is allowed to vary in the NPT simulations, elastic energy is taken into account in molecular dynamics simulations as well.) Therefore, a deviation from the preferred value of polarization automatically implies a change in the unit-cell parameters, and the energy of this change is included in our model as the local energy penalty (U_{loc}).

Analysis of the Miller–Weinreich nucleation model. The original work of Miller and Weinreich[15] (illustrated in Extended Data Fig. 4) is based on the following assumptions: (1) the nucleus boundary is oriented at a 90° angle relative to the original domain wall; (2) the nucleus is located at the surface of the material and has a net non-zero boundary charge ($\rho_1 + \rho_2 > 0$); (3) the boundary of the nucleus has the same interface energy as that of the planar domain wall (σ_w) on which the nucleus is located; and (4) the σ_p parameter that characterizes the strength of the depolarization interactions is large relative to the magnitude of the local interface energy characterized by σ_w. The assumption that $\sigma_p \gg \sigma_w$ leads to the triangular (red in Extended Data Fig. 4) nucleus shape.

Owing to the lack of reliable experimental or first-principles data for the domain-wall energy, the model was assumed to be correct in ref. 15 and so was used to parameterize the domain-wall energy with the available domain-wall velocity data. This allowed the fitting of the electric-field/domain-wall-velocity relationships in many experiments. Despite this success, two major studies have cast serious doubt on the model. First, first-principles calculations of domain-wall energy per unit area (σ_w) were found to be markedly higher than the fit values and, conversely, inserting the accurate, calculated values into the Miller–Weinreich model gave velocities that were markedly lower than those observed experimentally[9]. Second, multiscale modelling of the nucleation process on the domain wall for 180° domain walls shows that the critical nucleus is not a tall, narrow, sharp triangle, as suggested in ref. 15. Instead, the observed nucleus is a diffuse, bevelled square[17]. We show that rather than the $\sigma_p \gg \sigma_w$ limit assumed in ref. 15, the actual nucleation takes place in the $\sigma_w \gg \sigma_p$ limit, with the local interface energy playing the dominant role and governing the energetics of nucleation and growth.

Reduced depolarization energy. For simplicity, we discuss the relative energies of the depolarization and local interface terms adopting the triangular shape and form of the nucleus energy expression of ref. 15 (presented in Extended Data Fig. 4), so that these terms are discussed in the framework traditionally used to model nucleation on the domain wall. Four factors contribute to the reduced role of depolarization energy in nucleation.

First, the bevelled shape of the nucleus effectively reduces σ_w. Because the depolarization energy of the Miller–Weinreich model arises from the electrostatic interactions between the charges along the boundary of the nucleus, the magnitude of σ_p exhibits a logarithmic dependence on the width of the nucleus (a). Although the boundary of the nucleus was assumed to be sharp in ref. 15 and at a 90° angle to the domain wall, the actual nucleus boundary has a bevelled shape, as shown in previous molecular dynamics studies[17]. This decreases the effective domain-wall area or, alternatively, the effective local-domain-wall energy ($\sigma_{eff,w}$) for a given nucleus of width a. According to equation (9) in ref. 15 (also presented in Extended Data Fig. 4), the magnitude of the width of the critical nucleus a^* is determined by the ratio between σ_w and the PE terms in the limit $\sigma_p \gg \sigma_w$ and in the limit $\sigma_w \gg \sigma_p$. Thus, for all cases, a decrease in σ_w leads to a smaller critical width a^* and therefore a smaller critical depolarization energy σ_p^*. The logarithmic dependence of σ_p is not weak for the small nuclei observed in our molecular dynamics simulations. Therefore, a decrease in the local interface energy due to the bevelled shape of the nucleus, which favours smaller critical nucleus size, also substantially decreases the magnitude of σ_p^*.

Second, the dielectric constant is enhanced at the domain wall and therefore the screening at the domain wall is stronger than in the bulk of the material. Recent experimental[1] and theoretical work[33] has shown that the dielectric constant at the domain wall is larger than that in the bulk. This is confirmed by our molecular dynamics simulations that show that the local dipole fluctuations and therefore the dielectric constant at the 90° domain wall are enhanced by a factor of two relative to the bulk value. Owing to the presence of the dielectric constant in the denominator of the formula for σ_p, the actual σ_p value is then reduced by another factor of two relative to the original Miller–Weinreich estimate.

Third, the diamond shape of the nucleus shows an interaction cancellation effect. An additional effect is present for the elongated-diamond-like nuclei found in this work. Unlike the Miller–Weinreich model, which is not charge neutral, the elongated diamond shape observed in our molecular dynamics simulations exhibits both positive (ρ_1 and ρ_2) and negative ($-\rho_3$ and $-\rho_4$) boundary charges (Extended Data Fig. 5) so that the total charge at the nucleus boundary (Q_{tot}) is zero. Therefore, the repulsive energy penalty due to the interaction between ρ_1 and ρ_2, and between $-\rho_3$ and $-\rho_4$, is cancelled by the attractive energy gain of the interaction between ρ_1 and $-\rho_3$, and between ρ_2 and $-\rho_4$. This changes the dependence of σ_p on a from $\ln[2a/(eb)]$ to $\ln[(a/eb)]$ (the $4P_s^2 b/[\epsilon \ln(2)]$ contribution (in which ϵ is the dielectric constant) to σ_p (see Extended Data Fig. 4 for definitions of e and b) arises from the interaction between the charges on the two opposite sides of the triangle; see the text following equation (4) in ref. 15). Although this change would have a minor effect on the large nucleus assumed in ref. 15, it is highly important for the small nucleus observed in our molecular dynamics simulations.

Finally, the boundary of the nucleus has a much smaller depolarization charge. We find that the average boundary charge between the nucleus and the original domain as integrated from the polarization changes on the 90° domain wall observed in our molecular dynamics calculations (Extended Data Fig. 5) is about two times smaller ($\Delta P = 0.7 \, C\,m^{-2}$) than that predicted by the sharp polarization change ($\Delta P = 2P_s = 1.41 \, C\,m^{-2}$) that would be used in a Miller–Weinreich-like model. Such a small polarization change is due to the greatly decreased value of P_Y at the domain wall relative to the bulk value. First-principles calculations[16] show that the diffuseness of the 90° domain wall means that P_Y at the domain wall layer is only about 50% of the bulk value. This large decrease in P_Y is also found in our calculations (Fig. 2a). It is this domain wall layer that undergoes the nucleation and growth process governing the domain-wall motion, and therefore the appropriate value of P to be used for estimating the depolarization charge is much smaller than the Miller–Weinreich estimate based on the bulk value P_s. The much smaller charge generated at the boundary of the nucleus decreases the strength of electrostatic interactions and σ_p by a further factor of approximately four.

Despite the small σ_p, our nucleus still exhibits an elongated shape; this is due to the greater magnitude of the local energy σ_w for the domain wall at which P changes along the P direction than that for the domain wall at which P changes along a direction transverse to the P direction, as found in ref. 17 for 180°-domain-wall motion. This is also unlike the assumption in ref. 15 that σ_w is the same as the energy of the flat domain wall for all nucleus boundaries.

In summary, rather than the $\sigma_p \gg \sigma_w$ limit assumed in ref. 15, the actual nucleation takes place in the $\sigma_w \gg \sigma_p$ limit, with the local interface energy playing the dominant role and governing the energetics of nucleation and growth. This not only justifies our analytical model that neglects the small depolarization energy term, but also represents a new understanding of the physics that is important for ferroelectric switching.

Quantitative analysis of σ_p reduction. We quantitatively evaluate the impact of the effects described above (bevelled shape, high dielectric constant, cancellation effect and small depolarization charge) on the depolarization energy term (σ_p). To take the modification of the boundary structure into account, we write down a modified version of the Miller–Weinreich formula:

$$U_{nuc} = -2P_s Ealc + 2s\sigma_w c\sqrt{a^2 + l^2} + U_d$$

$$U_d = \frac{8f_c^2 P_s^2 c^2}{f_\epsilon \epsilon} \frac{a^2}{l} \ln\left(\frac{f_Q a}{eb}\right) = 2\sigma_p ba^2/l$$

$$\sigma_p = \frac{4f_c^2 P_s^2 c^2}{f_\epsilon \epsilon} \ln\left(\frac{f_Q a}{eb}\right) \qquad (5)$$

where σ_w is the energy of the planar 90° domain wall, $s = 0.41$ is a factor that accounts for the reduction in the interface area of the nucleus due to its bevelled shape, as described previously[17] ($\sigma_{eff,w} = s\sigma_w$), f_c is the scaling factor between the actual charge at the nucleus and the boundary charge assumed in the Miller–Weinreich model, f_ϵ is the scaling factor between the values of the dielectric constant (ϵ) at the domain wall and in the bulk, and f_Q is a factor reflecting the effect of the interactions between the charged domain boundaries at the net-neutral ($Q_{tot} = 0$) and net-charged ($Q_{tot} \neq 0$) boundaries of the nucleus, with $f_Q = 2$ for the original, charged, triangular, Miller–Weinreich nucleus and $f_Q = 1$ for a net-neutral, diamond-like nucleus.

To determine the dimensions and the energy of the critical nucleus, we evaluate U_{nuc} for a wide range of a and l values and identify those that give the lowest energy for each nucleus area $A = al$. Here, we use the DFT σ_w value of 35 mJ m^{-2} for the 90° domain wall and standard parameters for PbTiO$_3$ (dielectric constant $\epsilon = 60$, bulk polarization component in the plane of the 90° domain wall $P_s = 0.53 \, C\,m^{-2}$, $b = 3.9 \, Å$, $c = 4 \, Å$ and $e = 2.718$). The plots of the nucleus energy versus area (A) for different values of s, f_c, f_ϵ and f_Q under an applied field of 0.1 MV cm^{-1}, which is typical of the low range of field magnitudes used in molecular dynamics simulations, are shown in Extended Data Fig. 6. We also show the dependence of the nucleus aspect ratio (l^*/a^*, where l^* is the length of critical nucleus; see Extended Data Fig. 5) on the ratio of σ_p and σ_w, and the σ_p values obtained for different values of s, f_c, f_ϵ and f_Q.

Examination of Extended Data Fig. 6 shows several important differences between the results of the classical Miller–Weinreich approach and the results obtained for a Miller–Weinreich-like nucleus with realistic boundaries. First, even for $s = f_c = f_\epsilon = 1$, the obtained $a^* = 12.5b$ and $l^* = 47b$ values are relatively small. For such a small a^*, the dependence of σ_p on $\ln[(a/(eb)]$ is not weak and, therefore, reduction of a^* due to the effects described above (smaller effective domain-wall area due to bevelled shape) has a strong effect on σ_p. Taken together, the various effects lead to a reduction in σ_p by a factor of about 30 relative to the Miller–Weinreich estimate for nucleation at the 90° domain wall under an applied field of 0.1 MV cm^{-1}. This results in $\sigma_p \approx 5.7$ mJ cm^{-2}, much smaller than the local interface energy characterized by the effective domain-wall energy $\sigma_{eff,w} = 15.4$ mJ cm^{-2}. The small value of σ_p justifies our neglect of electrostatic interactions in the analytical model of the nucleus, and the much smaller σ_p/σ_w ratio corresponds to an aspect ratio of the critical nucleus (l^*/a^*) that is close to one.

As illustrated in Extended Data Fig. 7, similar effects can be obtained for nucleation on the 180° domain wall under an applied field of 0.3 MV cm^{-1} using the DFT 180°-domain-wall σ_w value of 132 mJ m^{-2} and standard parameters for PbTiO$_3$ (dielectric constant $\epsilon = 60$, bulk polarization $P_s = 0.75 \, C\,m^{-2}$, $b = 3.9 \, Å$, $c = 4 \, Å$ and $e = 2.718$).

Model parameters for non-180° domain walls. The nucleation model discussed here is similar to the model in ref. 17. The mapping scheme discussed therein allows the treatment of a non-180° domain wall as a generalized 180° domain wall lying in the Y–Z plane with polarization changing from $+P_Y$ to $-P_Y$ along X. The following five parameters are required to estimate the nucleation energy at the domain wall under a given temperature T: $P_s(T)$, $A_{loc}(T)$, g_{YY}, g_{YX} and g_{YZ}, where:

$$P_Y(T) = \gamma P_s(T)$$

$$A_{loc}(T) = A_{loc}(0)\frac{P_s^4(T)}{P_s^4(0)}$$

$$A_{loc}^Y(0) = \gamma^4 A_{loc}(0)$$

$$g_{YX} \approx g_{YZ} = \left[\frac{3\sigma_{DW}^{YX}}{8P_Y(0)}\right]^2 \frac{1}{A_{loc}^Y(0)} = A_{loc}^Y(0)\left[\frac{\delta_X}{2P_Y(0)}\right]^2$$

$$g_{YY} = \left[\frac{3\sigma_{DW}^{YY}}{8P_Y(0)}\right]^2 \frac{1}{A_{loc}^Y(0)} = A_{loc}^Y(0)\left[\frac{\delta_Y}{2P_Y(0)}\right]^2$$

Here P_s is the total local polarization, γ is the fraction of the polarization variation across the domain boundary (for example, $\gamma = \sqrt{2}/2$ for a 90° domain wall), A_{loc} is the energy difference between the ferroelectric phase and the high-symmetry paraelectric phase, σ_{DW}^{YX} is the energy of a domain wall with normal along X and neighbouring dipoles along Y, and δ_X is the polarization diffuseness parameter over which the polarization changes across the domain boundary. By analogy, σ_{DW}^{YY} is the energy of a domain wall with normal along Y and neighbouring dipoles along Y (head-to-head or tail-to-tail domain wall), and δ_Y is the associated diffuseness parameter. $P_s(0)$ and $A_{loc}(0)$ are extracted from zero-kelvin DFT calculations. The temperature dependence of $P_s(T)$ is taken from experiments when available. The values of g_{YY} and g_{YZ} can be determined on the basis of the domain-wall energy (σ_{DW}, calculated from DFT) or diffuseness parameters (δ, calculated from molecular dynamics). In practice, g_{YY}, g_{YX} and g_{YZ} are of the same order and therefore $g_{YX} \approx g_{YY}$ is a useful approximation.

For BaTiO$_3$, DFT calculations using the PBEsol density functional[34] with $a = 3.986$ Å and $c/a = 1.01$ give $A_{loc}(0) = 3.48 \times 10^7\,\mathrm{J\,m^{-3}}$, $\sigma_{180DW} = 11\,\mathrm{mJ\,m^{-2}}$, $\sigma_{90DW} = 3.89\,\mathrm{mJ\,m^{-2}}$, $P_s(0) = 0.283\,\mathrm{C\,m^{-2}}$ and $g_{YX} = 0.61 \times 10^{-11}\,\mathrm{m^3\,F^{-1}}$. These parameters are used for simulating the hysteresis loop in Fig. 3b. For PbTiO$_3$, we use experimental lattice constants ($a = 3.9$ Å and $c = 4.15$ Å) for DFT calculations with PBEsol and obtain $A_{loc}(0) = 5.05 \times 10^8\,\mathrm{J\,m^{-3}}$, $\sigma_{180DW} = 175\,\mathrm{mJ\,m^{-2}}$, $\sigma_{90DW} = 67\,\mathrm{mJ\,m^{-2}}$, $g_{YX} = 1.21 \times 10^{-11}\,\mathrm{m^3\,F^{-1}}$. The temperature dependence of polarization is taken from ref. 35, with $P_s(0) = 0.872\,\mathrm{C\,m^{-2}}$. These parameters are used for predicting the coercive fields of PbTiO$_3$-based ceramics and thin films in Fig. 3a, c.

LGD model for BiFeO$_3$ and other rhombohedral ferroelectrics with O$_6$ rotations. 71°, 109° and 180° domain walls are all observed in BiFeO$_3$. The energetics of these three types of domain walls have been investigated with DFT in several studies[36–38]. In ref. 36, $\sigma_{71DW} = 152\,\mathrm{mJ\,m^{-2}}$, $\sigma_{109DW} = 62\,\mathrm{mJ\,m^{-2}}$ and $\sigma_{180DW} = 73\,\mathrm{mJ\,m^{-2}}$ was reported using LDA+U. In ref. 38, $\sigma_{71DW} = 128\,\mathrm{mJ\,m^{-2}}$, $\sigma_{109DW} = 33\,\mathrm{mJ\,m^{-2}}$ and $\sigma_{180DW} = 98\,\mathrm{mJ\,m^{-2}}$ was reported with GGA+U. From equation (5), we deduce that $\sigma_{DW}^{YX} \propto P_Y\sqrt{A_{loc}^Y g_{YX}}$. Assuming the polarization gradient coefficient is isotropic, the energy of a non-180° domain wall (σ_{DW}^γ) can be related to that of a 180° domain wall: $\sigma_{DW}^\gamma = \gamma^3\sigma_{180DW}$. Therefore, for a given ferroelectric, $\sigma_{71DW}{:}\sigma_{90DW}{:}\sigma_{109DW}{:}\sigma_{180DW} = 0.192{:}0.354{:}0.544{:}1$. This relationship works well for 90° and 180° domain walls in BaTiO$_3$ and PbTiO$_3$ (ref. 16), and reasonably well for 109° and 180° domain walls in BiFeO$_3$ (refs 36, 38). However, the 71° domain wall is found to have the highest energy in BiFeO$_3$, which is attributed to the mismatch of oxygen octahedral rotation across the domain boundary[36,38]. To capture this feature, we introduce a second order parameter, oxygen octahedra rotation (Θ), into the LGD model of BiFeO$_3$. Therefore, the 71° domain wall in BiFeO$_3$ has the following extra energy term:

$$U_\Theta = \frac{1}{2}K\int_{-\infty}^{\infty}dX\int_{-\infty}^{\infty}dY\int_{-\infty}^{\infty}dZ[\Theta_{DW}(X,Y,Z) - \Theta_{bulk}(X,Y,Z)]$$

where K is the harmonic angle constant and $\Theta_{bulk}(X,Y,Z) \approx 8°$ (ref. 38). The value of K ($6.106 \times 10^9\,\mathrm{J\,m^{-3}\,rad^{-2}}$) is optimized such that the LGD model reproduces the DFT value of σ_{71DW} with the gradient coefficient ($g_{YX} = 0.32 \times 10^{-11}\,\mathrm{m^3\,F^{-1}}$) estimated from σ_{109DW}. The following term is then added to equation (3) when estimating the nucleation energy:

$$\Delta U_\Theta = \frac{1}{2}K\int_{-\infty}^{\infty}dX\int_{-\infty}^{\infty}dY\int_{-\infty}^{\infty}dZ[\Theta_{nuc}(X,Y,Z) - \Theta_{DW}(X,Y,Z)]$$

where an analytical equation similar to equation (4) is used to describe the angle profile $\Theta_{nuc}(X,Y,Z)$. Other parameters are $A_{loc}(0) = 5.81 \times 10^8\,\mathrm{J\,m^{-3}}$, $P_s(0) = 0.987\,\mathrm{C\,m^{-2}}$ and $T_0 = 1{,}120\,\mathrm{K}$.

Coarse-grained simulation of P–E hysteresis loop. The coercive field reflects the ease of domain reversal and is one of the most important characteristic parameters of ferroelectrics for practical applications. For the domain-reversal process achieved via domain-wall motion, the change in the polarization under an applied electric field directly correlates with the distance moved by the domain wall, the velocity of which can be estimated using Merz's law. We extract the pre-exponential

factor v_0 in Merz's law from molecular dynamics simulations in the creep-like region and obtain E_a for PbTiO$_3$ from the LGD model with parameters calculated with DFT PBEsol[39]. With these values of v_0 and E_a, we then simulate the hysteresis loops at 300 K and obtain the frequency dependence of E_c for varying domain sizes (Fig. 3a). Following the experimental set-up used in most hysteresis-loop measurements, a triangular electric field $E(t)$, with frequency f, maximum magnitude E_0 and time t, is used in the simulation:

$$E(t) = \begin{cases} 4fE_0t & 0 < t < \dfrac{1}{4f} \\[2mm] -4fE_0t + 2E_0 & \dfrac{1}{4f} < t < \dfrac{3}{4f} \\[2mm] 4fE_0t - 4E_0 & \dfrac{3}{4f} < t < \dfrac{1}{f} \end{cases}$$

At $t = 0$, the domain of size d is fully poled with saturation polarization $-P_s$. Assuming the domain reversal is achieved via domain-wall motion, the polarization at time t can be calculated using:

$$P(t) = -P_s + \frac{\int_0^{1/f} v(t)\,dt}{d}P_s \tag{6}$$

where $v(t)$ is the domain-wall velocity at time t and is calculated using Merz's law: $v(t) = v_0\exp[-E_a/E(t)]$. When the value of $P(t)$ obtained from equation (6) is larger than P_s (such that the domain is already fully reversed), $P(t)$ is set to P_s. Plotting $P(t)$ with respect to $E(t)$ gives the hysteresis loop. The coercive field E_c is the magnitude of the electric field when $P(t) = 0$. On the basis of the molecular dynamics simulation results, we used $v_0 = 300\,\mathrm{m\,s^{-1}}$ for predicting room-temperature coercive fields. We find that the coercive field is not sensitive to the value of v_0, as demonstrated by the moderate change in coercive fields in response to orders of magnitude change in d (which is equivalent to changing v_0 for fixed d) shown in Fig. 3. This indicates that the magnitude of the coercive field is largely determined by the activation field.

Comparison of coercive fields for tetragonal and rhombohedral ferroelectrics. The values of P_s, $A_{loc}(0)$, σ_{90DW}, g_{YX} and g_{YX} are derived from PbTiO$_3$. These parameters are used for simulating the hysteresis loop and coercive field of tetragonal (T) ferroelectrics. The value of σ_{71DW} is estimated as $0.542\sigma_{90DW}$ (as explained above). To account for the possible octahedral rotations across the 71° domain wall, we use the angle constant derived from BiFeO$_3$ when simulating the coercive field for rhombohedral (R) ferroelectrics; we find that $E_c^T/E_c^R \approx 1.8$.

Effect of supercell size. We carried out a benchmark study on the effect of supercell size (Extended Data Fig. 8). We calculated the domain-wall velocity with $40 \times 40 \times 40$, $50 \times 50 \times 40$, $60 \times 60 \times 40$ and $65 \times 65 \times 40$ supercells at 200 K and 240 K. The key finding is that the values obtained with the $40 \times 40 \times 40$ supercell do not substantially deviate from values found using the larger supercells (within $10\,\mathrm{m\,s^{-1}}$). Most importantly, the v_x–E slope is similar for supercells of different sizes, showing that the domain-wall dynamics obtained with a $40 \times 40 \times 40$ supercell are robust against supercell size.

31. Shin, Y.-H., Cooper, V. R., Grinberg, I. & Rappe, A. M. Development of a bond-valence molecular-dynamics model for complex oxides. *Phys. Rev. B* **71**, 054104 (2005).
32. Jablonski, M. L. *et al.* Asymmetric response of ferroelastic domain-wall motion under applied bias. *ACS Appl. Mater. Interfaces* **8**, 2935–2941 (2016).
33. Wojdeł, J. C. & Íñiguez, J. Ferroelectric transitions at ferroelectric domain walls found from first principles. *Phys. Rev. Lett.* **112**, 247603 (2014).
34. Perdew, J. P. *et al.* Restoring the density-gradient expansion for exchange in solids and surfaces. *Phys. Rev. Lett.* **100**, 136406 (2008).
35. Rossetti, G. A. Jr, Cline, J. P. & Navrotsky, A. Phase transition energetics and thermodynamic properties of ferroelectric PbTiO$_3$. *J. Mater. Res.* **13**, 3197–3206 (1998).
36. Diéguez, O., Aguado-Puente, P., Junquera, J. & Íñiguez, J. Domain walls in a perovskite oxide with two primary structural order parameters: first-principles study of BiFeO$_3$. *Phys. Rev. B* **87**, 024102 (2013).
37. Ren, W. *et al.* Ferroelectric domains in multiferroic BiFeO$_3$ films under epitaxial strains. *Phys. Rev. Lett.* **110**, 187601 (2013).
38. Wang, Y. *et al.* BiFeO$_3$ domain wall energies and structures: a combined experimental and density functional theory + U study. *Phys. Rev. Lett.* **110**, 267601 (2013).
39. Zhao, Y. & Truhlar, D. G. Construction of a generalized gradient approximation by restoring the density-gradient expansion and enforcing a tight Lieb–Oxford bound. *J. Chem. Phys.* **128**, 184109 (2008).
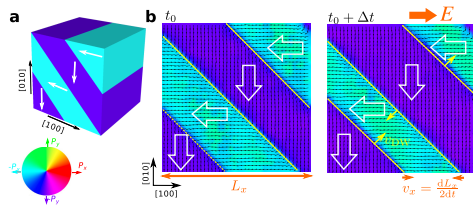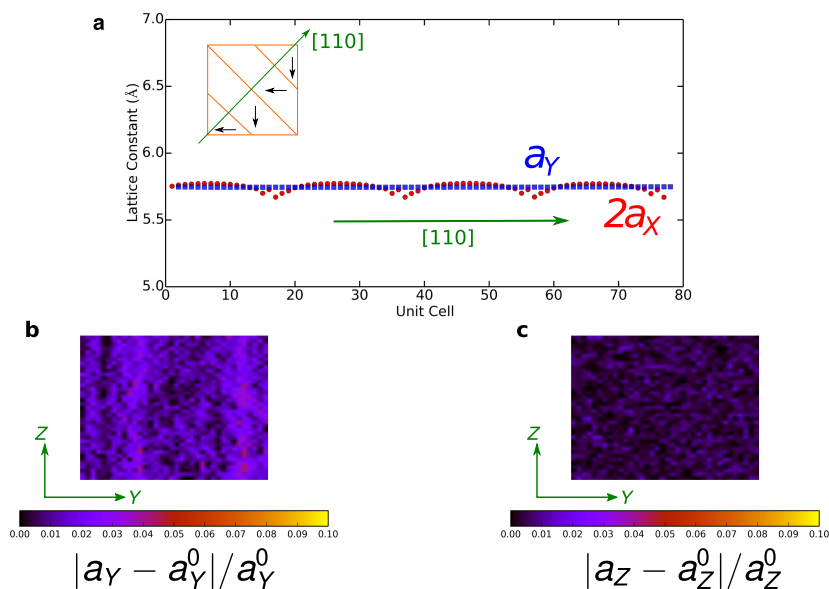
Extended Data Figure 1 | Large-scale molecular dynamics simulations of 90°-domain-wall motions. a, Schematic of a $40 \times 40 \times 40$ supercell with 90° domain walls used in molecular dynamics simulations. The colours of the domains correspond to the polarization (P) wheel shown at the bottom. White arrows represent the polarization directions of domains. **b**, Simulated domain evolution under a [100]-oriented electric field (E). The dashed yellow lines show the positions of 90° domain walls. The electric field is turned on at time t_0. The domain-wall velocity v_{DW} along [110] (yellow arrows) is estimated on the basis of the change in the supercell dimension (L_x) along [100] from t_0 to $t_0 + \Delta t$. The black arrows scale with the local dipole of each unit cell. The domain wall motion is achieved via the 90° switching of $[\bar{1}00]$ dipoles to $[0\bar{1}0]$ dipoles.
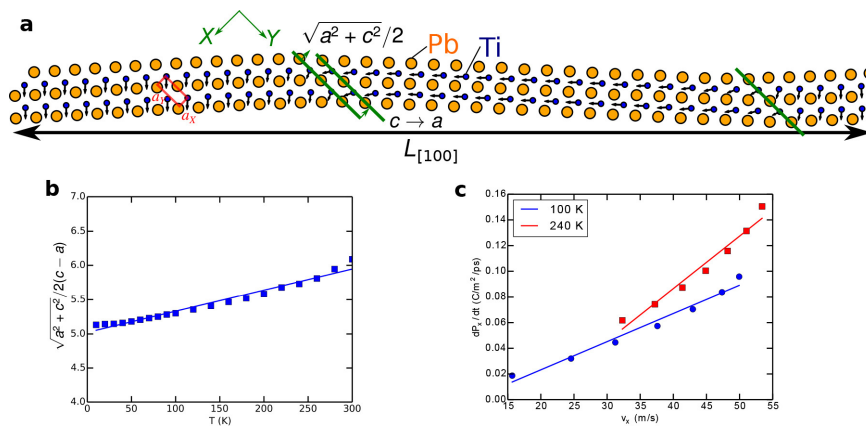
Extended Data Figure 2 | Lattice constants of supercells used in molecular dynamics simulations. a, Pb (orange) and Ti (blue) sublattices in a $PbTiO_3$ supercell with 90° domain walls. The boundaries are marked by green lines. a_X and a_Y are effective lattice constants of the domain-wall unit cell defined in the transformed X–Y coordinates and shown by the red rectangle. When dipoles in one layer of unit cells switch by 90° ($c \to a$), the wall moves by $(a^2 + c^2)^{1/2}/2$ along the [110] direction. **b**, Temperature (T) dependence of $\sqrt{a^2 + c^2}/[2(c - a)]$ obtained from molecular dynamics simulations (squares). It depends on temperature weakly (blue line). **c**, Plot of polarization change (dP_x/dt) versus cell-dimension change (v_x). The solid curves show linear fits at 100 K (blue) and 240 K (red).

Extended Data Figure 3 | Elastic energy contribution to nucleation energy. a, Effective lattice constants across 90° domain walls. The inset is the top view of the $40 \times 40 \times 40$ supercell used in molecular dynamics simulations; black arrows indicate the polarization direction. The effective lattice constants (a_X and a_Y) are defined in X–Y coordinates, as explained in Extended Data Fig. 1. The averaged lattice constants for each layer of cells across the domain wall along the [110] direction are plotted. **b, c**, Distributions of strain gradient at the domain wall in the presence of a nucleus. a_Y^0 and a_Z^0 are the effective lattice constants along Y and Z in the absence of nucleus ($t = 0$ ps in molecular dynamics simulations), respectively.

Nucleation Energy
$$U_{\text{nuc}} = -2P_s Ealc + 2\sigma_w c(a^2 + l^2)^{\frac{1}{2}} + U_d$$

Depolarization Energy
$$U_d = 8P_s^2 \frac{c^2}{\epsilon} \frac{a^2}{l} \ln \frac{2a}{eb} = 2\sigma_p ba^2/l$$

$$\sigma_p = 4P_s^2 \frac{b}{\epsilon} \ln \frac{2a}{eb}$$

Dimensions of critical nucleus
$$a^* = \frac{\sigma_w}{P_s E} \frac{\sigma_w + 2\sigma_p}{\sigma_w + 3\sigma_p} \qquad \frac{a^*}{l^*} = \frac{\sigma_w^{\frac{1}{2}}}{(\sigma_w + 3\sigma_p)^{\frac{1}{2}}}$$

$$l^* = \frac{\sigma_w^{\frac{1}{2}}}{P_s E} \frac{\sigma_w + 2\sigma_p}{(\sigma_w + 3\sigma_p)^{\frac{1}{2}}}$$
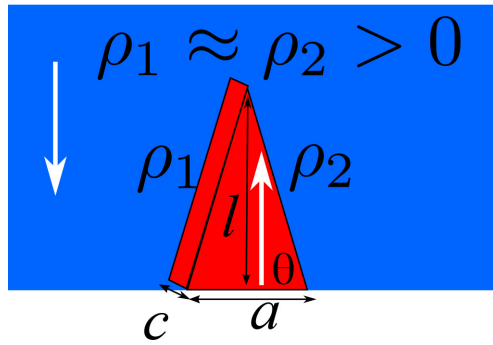
Extended Data Figure 4 | Schematic of a triangular-shaped nucleus, as in the Miller–Weinreich model. The triangular-shaped nucleus (red) has a polarization direction (white arrows) that is antiparallel to its neighbouring domains (blue). The depolarization charges $\rho_{1,2}$ at two boundaries are of the same sign, giving rise to repulsive energy penalty. The expressions for nucleation energy (U_{nuc}), depolarization energy (U_d), depolarization-contributed domain-wall energy (σ_p) and the dimensions for the critical nucleus a^* and l^* are taken from the original work of Miller and Weinreich, ref. 15; c and b are lattice constants ($c \approx b$ in PbTiO$_3$ and BaTiO$_3$), e is the base of natural logarithm, and ϵ is the dielectric constant. The σ_p/σ_w ratio determines the aspect ratio of the critical nucleus (l^*/a^*).

a

dP_Y/dY (C/m²/Å)

b

dP_Y/dZ (C/m²/Å)
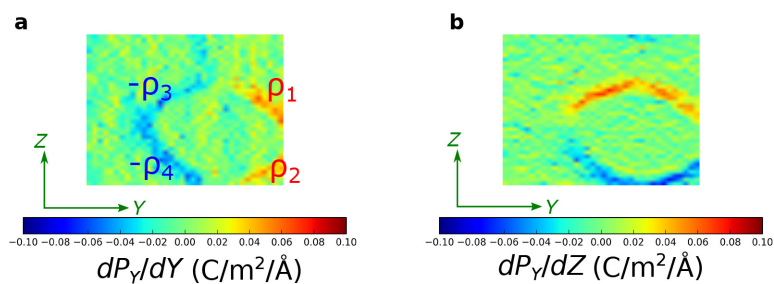
Extended Data Figure 5 | Distributions of polarization gradient at the domain wall in the presence of a nucleus. a, b, The polarization gradients (dP_Y/dY, **a**; dP_Z/dZ, **b**) are highest at the boundary of the nucleus. The maximum polarization gradient is around $0.08\,\mathrm{C\,m^{-2}\,Å^{-1}}$, much smaller than the value estimated by the classical theories in ref. 15 ($0.25\,\mathrm{C\,m^{-2}\,Å^{-1}}$). This difference is due to the diffuse nature of the boundary. The total boundary charge ($\rho_1 + \rho_2 + \rho_3 + \rho_4$) is zero.
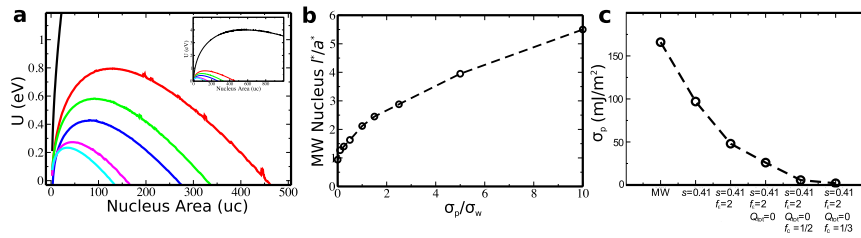
**Extended Data Figure 6 | Results for the Miller–Weinreich model of nucleation on the PbTiO₃ 90° domain wall using various conditions for the interface boundary. a**, Nucleus energy U as a function of Miller–Weinreich nucleus area (al, given in terms of the number of unit cells (uc)) for the original Miller–Weinreich model (black) and Miller–Weinreich models with $s = 0.41$, $f_\epsilon = 1$, $Q_{tot} \neq 0$ and $f_c = 1$ (red), $s = 0.41$, $f_\epsilon = 2$, $Q_{tot} \neq 0$ and $f_c = 1$ (green), $s = 0.41$, $f_\epsilon = 2$, $Q_{tot} = 0$ and $f_c = 1$ (blue), $s = 0.41$, $f_\epsilon = 2$,

$Q_{tot} = 0$ and $f_c = 1/2$ (magenta), and $s = 0.41$, $f_\epsilon = 2$, $Q_{tot} = 0$ and $f_c = 1/3$ (cyan). Inset, zoomed-out view showing all the curves. **b**, Aspect ratio of the Miller–Weinreich nucleus (l^*/a^*) as a function of the ratio between σ_p and σ_w. The Miller–Weinreich assumption that $l^* \gg a^*$ is not valid for realistic values of σ_p and σ_w. **c**, σ_p for different interface conditions. The actual σ_p is much smaller than the estimate used by Miller and Weinreich (MW; ref. 15).
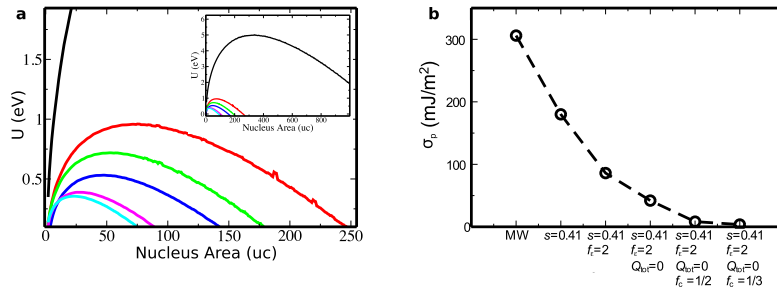
Extended Data Figure 7 | Results for the Miller–Weinreich model of nucleation on the PbTiO₃ 180° domain wall using various conditions for the interface boundary. a, Nucleus energy U as a function of Miller–Weinreich nucleus area (*al*, given in terms of the number of unit cells (uc)) for the original Miller–Weinreich model (black) and Miller–Weinreich models with $s = 0.41$, $f_\epsilon = 1$, $Q_{tot} \neq 0$ and $f_c = 1$ (red), $s = 0.41$, $f_\epsilon = 2$,

$Q_{tot} \neq 0$ and $f_c = 1$ (green), $s = 0.41$, $f_\epsilon = 2$, $Q_{tot} = 0$ and $f_c = 1$ (blue), $s = 0.41$, $f_\epsilon = 2$, $Q_{tot} = 0$ and $f_c = 1/2$ (magenta), and $s = 0.41$, $f_\epsilon = 2$, $Q_{tot} = 0$ and $f_c = 1/3$ (cyan). Inset, zoomed-out view showing all the curves. **b**, σ_p for different interface conditions. The actual σ_p is much smaller than the estimate used by Miller–Weinreich (MW; ref. 15).
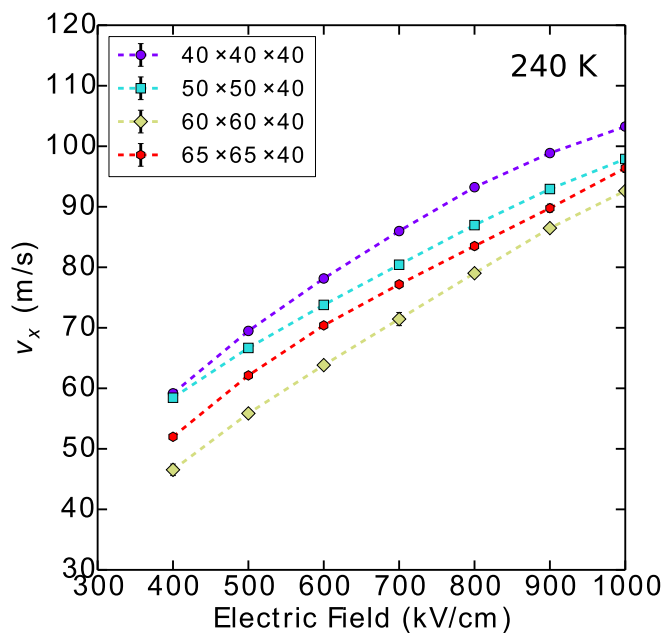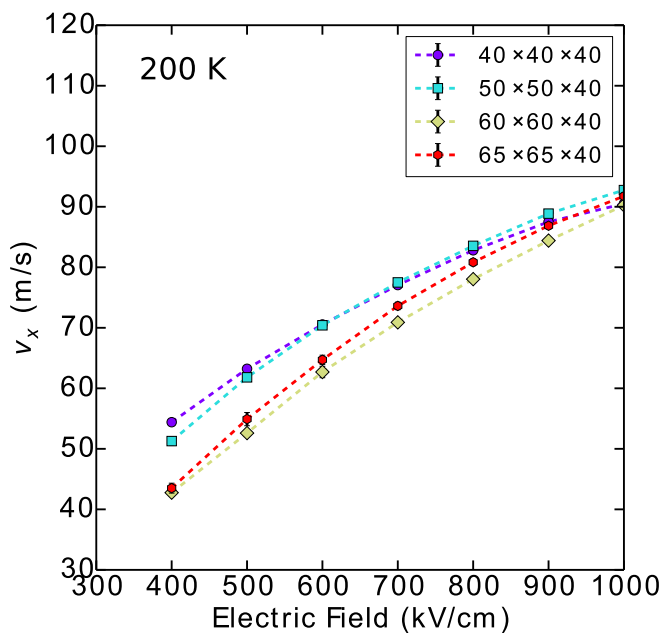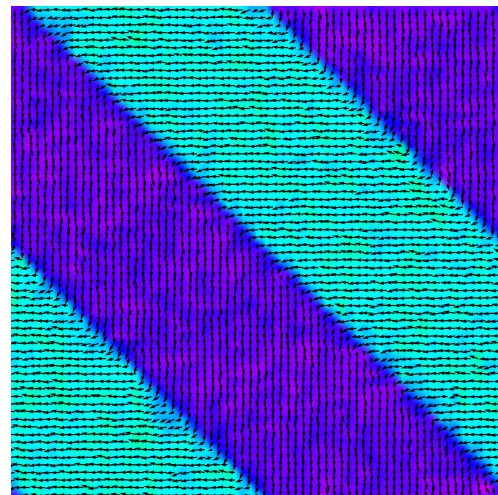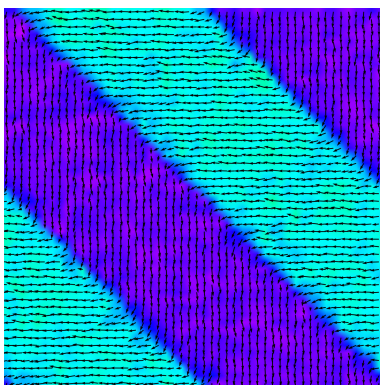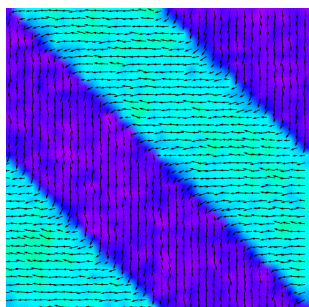
Extended Data Figure 8 | Test of domain-wall velocity (v_x) convergence with supercell size. The colours of the domains in the bottom panels correspond to those in Extended Data Fig. 1. The error bars are standard deviations.